PCCP

Role of Ring-Enlargement Reactions in the Formation of Aromatic Hydrocarbons

Journal:	*Physical Chemistry Chemical Physics*
Manuscript ID	CP-ART-10-2019-005854.R1
Article Type:	Paper
Date Submitted by the Author:	16-Jan-2020
Complete List of Authors:	Baroncelli, Martina; RWTH Aachen University, Institute for Combustion Technology Mao, Qian; RWTH Aachen University, Institute for Combustion Technology Galle, Simon; RWTH Aachen University, Institute for Combustion Technology Hansen, Nils; Sandia National Laboratories, Combustion Research Facility Pitsch, Heinz; Institute for Combustion Technology

ARTICLE

Role of Ring-Enlargement Reactions in the Formation of Aromatic Hydrocarbons†

Received 00th January 20xx,
Accepted 00th January 20xx

DOI: 10.1039/x0xx00000x

Martina Baroncelli,[a] Qian Mao,[a] Simon Galle,[a] Nils Hansen,[b] and Heinz Pitsch[a]

Ring-enlargement reactions can provide a fast route towards the formation of six-membered single-ring or polycyclic aromatic hydrocarbons (PAHs). To investigate the participation of the cyclopentadienyl (C_5H_5) radical in ring-enlargement reactions in high-temperature environments, a mass-spectrometric study was conducted. Experimental access to the C_5H_5 high-temperature chemistry was provided by two counterflow diffusion flames. Cyclopentene was chosen as a primary fuel given the large amount of the resonantly stabilized cyclopentadienyl radicals produced by its decomposition and its high tendency to form PAHs. In a second experiment, methane was added to the fuel stream to promote methyl addition pathways and to assess the importance of ring-enlargement reactions for PAH growth. The experimental dataset includes mole fraction profiles of small intermediate hydrocarbons and of several larger species featuring up to four condensed aromatic rings. Results show that, while the addition of methane enhances the production of methylcyclopentadiene and benzene, the concentration of larger polycyclic hydrocarbons is reduced. The increase of benzene is probably attributable to the interaction between the methyl and the cyclopentadienyl radicals. However, the formation of larger aromatics seems to be dominated only by the cyclopentadienyl driven molecular-growth routes which are hampered by the addition of methane. In addition to the experimental work, two chemical mechanisms were tested and newly calculated reaction rates for cyclopentadiene reactions were included. In an attempt to assess the impact of cyclopentadienyl ring-enlargement chemistry on the mechanisms' predictivity, pathways to form benzene, toluene, and ethylbenzene were investigated. Results show that the updated mechanism provides an improved agreement between the computed and measured aromatics concentrations. Nevertheless, a detailed study of the single reaction steps leading to toluene, styrene, and ethylbenzene would be certainly beneficial.

1. Introduction

The kinetics of aromatic hydrocarbon formation in extreme environments remains an intriguing research topic that receives continuous attention in the fields of astrochemistry and combustion science.[1, 2] Much theoretical and experimental work has been performed to understand the formation of single-ring aromatic hydrocarbons and their subsequent growth to polycyclic aromatic hydrocarbons (PAHs) at low and high temperatures.[3-5]

It is now accepted that the formation of the single-ring aromatic species often involves resonantly stabilized radicals such as propargyl ($HCCCH_2$), allyl (CH_2CHCH_2), *i*-C_4H_5 (CH_2CHCCH_2), and cyclopentadienyl (C_5H_5).[6] Especially the latter radical has been hypothesized to have a multifaceted chemistry that can involve decomposition to $C_3H_3 + C_2H_2$, self-reaction with another C_5H_5 radical to form naphthalene + 2H, and reactions with CH_3, C_2H_2, and C_3H_3 to form C_6H_6+2H, C_7H_7 radicals, and C_8H_8 aromatics, respectively:

$$C_5H_5 \rightleftarrows C_3H_3 + C_2H_2 \quad (1)$$

$$C_5H_5 + C_5H_5 \rightarrow C_{10}H_8 + 2H \quad (2)$$

$$C_5H_5 + CH_3 \rightarrow C_6H_6 + 2H \quad (3)$$

$$C_5H_5 + C_2H_2 \rightleftarrows C_7H_7 \quad (4)$$

$$C_5H_5 + C_3H_3 \rightleftarrows C_8H_8 \quad (5)$$

The recombination of two C_5H_5 radicals (Eq. 2) and its potential to form naphthalene has been the focus of numerous works. This route would in fact allow to bypass the formation of single-ring aromatic species by directly forming naphthalene, the simplest PAH. As stated by Mebel et al.,[7] a detailed understanding of naphthalene formation channels via this route impels the study of several potential energy surfaces (PESs), which were performed by Wang et al.,[8] Cavallotti et al.,[9, 10] and Kislov and Mebel.[11] A recently performed pressure-dependence analysis by Long et al.[12] summarizes the most promising pathways for high and low temperatures. At high temperatures, formation of naphthalene and two H radicals seems

[a] Institute for Combustion Technology, RWTH Aachen University, Templergraben 64, 52062 Aachen, Germany.
[b] Combustion Research Facility, Sandia National Laboratories, Livermore, CA 94551, USA. Email: nhansen@sandia.gov

† Electronic Supplementary Information (ESI) available. See DOI: 10.1039/x0xx00000x

to be the most likely reaction, although the formation of other $C_{10}H_8$ isomers like fulvalene cannot be excluded.

Equations (3)-(5) represent so-called ring-enlargement reactions (RERs) as they efficiently can convert a five-membered ring into a six-membered (aromatic) ring. The possibility for ring-enlargements from C_5H_5 towards benzene (Eq. 3) via methyl (CH_3) radical addition was first explored by Melius et al.[13] and Moskaleva et al.[14] In its basic form, this sequence includes the formation of the methylcyclopentadienyl radical, followed by H elimination and β-scission to form fulvene, and a final isomerization reaction to obtain benzene (C_6H_6). A similar pathway was introduced by Laskin and Lifshitz[15] to model the formation of naphthalene starting from methyl addition to indenyl radical (C_9H_7). This reaction sequence has been recently experimentally verified by Zhao et al.,[16] opening new opportunities for further validation studies.

The insertion of acetylene into the C_5H_5 ring (Eq. 4) was proposed by Fascella et al.[17] as a route to form cycloheptatrienyl (c−C_7H_7) radicals. This channel was later experimentally confirmed,[18] and the possibility of an isomerization of c-C_7H_7 into the benzyl radical (C_7H_7) was explored. It was shown that the formation of C_7H_7 along this channel is a concrete possibility, thus providing a plausible route to form toluene (C_7H_8).

Along with these most-investigated pathways of the cyclopentadienyl radical, several other reactions forming other aromatics such as indene (C_9H_8) or styrene (C_8H_8, Eq. 5) have been proposed.[19, 20] However, these studies were mostly based on *ab initio* calculations and experimental datasets which could be useful to discriminate the most relevant reactions are still scarce.

The goal of this study is to elucidate the importance of ring-enlargement reactions at high temperatures as found, for example, in combustion environments. In combustion chemistry research, one convenient way to produce significant amounts of C_5H_5 is via oxidation of cyclopentene (C_5H_8). Given its chemical structure and its decomposition reactions, cyclopentene offers the possibility to examine in depth the above-mentioned aromatic formation routes. Cyclopentene oxidation has been studied to determine kinetic parameters and ignition delay times in shock tube and very low-pressure pyrolysis (VLPP) reactors.[21, 22] Premixed flames, non-premixed flames, and jet-stirred reactor (JSR) configurations were also employed in combination with different analytic techniques to enable the identification of stable and unstable species, as well as isomer discrimination.[23-29] All these studies underlined the fundamental role of the cyclopentadienyl radical for PAH and soot formation in high-temperature environments.

For this work, we have chosen a counterflow flame configuration fueled by cyclopentene, to which a significant amount of methane was added. By following this approach, important conclusions about the relevance of traditional mass growth reaction sequences in comparison with the above-mentioned ring-enlargement reactions were drawn, especially concerning the C_5H_5 + CH_3 channel (Eq. 3). In addition, this study includes theoretical and modeling components which provide additional support to the interpretation of the experimental results.

2. Experimental setup and data reduction

The experimental setup has been extensively described in previous works.[30, 31] Therefore, this section provides just a concise overview.

The counterflow burner consists of two vertically aligned coaxial stainless-steel nozzles with exit diameters of 30 mm. The axial alignment of the two opposed sections is obtained through manual adjustment and the vertical translation of the assembly is achieved through a computer-controlled stepper motor. The two nozzles were kept 23 mm apart, the oxidizer stream was supplied from the bottom nozzle, and the fuel was injected from the top. To avoid the impact of the environmental air on the combustion process, the fuel and the oxidizer nozzle were shielded through a 3 mm thick coaxial argon stream. To perform an active control of the pressure, which for these measurements was set to 60 Torr (80 mbar), the burner assembly was enclosed in a stainless-steel vessel.

Samples from different axial positions were extracted at the burner centerline via a horizontally mounted quartz conical probe[30] and guided into the ionization chamber by a nickel skimmer. A differently pumped vacuum system ensured the necessary low pressure (10^{-5} mbar) to expand the gas and form a molecular beam. The analyte was then ionized (at 10^{-7} mbar) by electrons with an energy probability density function characterized by a full width at half maximum (FWHM) of 2.2 eV. Mass separation was achieved by a Wiley-McLaren two stage pulsed ion extraction section[32] which, in combination with a two-stage reflectron, provided a mass resolution m/Δm of 3700. After separation, ions were detected by a microchannel plate (MCP) and signals recorded by a multichannel scaler (FAST MCS 65A). Given its high resolution, the mass spectrometer allowed for an unambiguous determination of the elemental composition (C/H/O) in the mass range of interest.

Starting from the recorded mass spectra, the data reduction procedures allow for the determination of the spatially resolved species mole fractions.[31, 33] Briefly, the conversion of the signal into a mole fraction requires the knowledge of several apparatus and species-specific parameters, which were obtained from machine characterization and from the available literature. However, this process entails some approximations and suffers from lack of literature data both leading to high uncertainties. Therefore, when possible, some of these parameters were substituted by the direct measurement of species calibration factors. In addition, probe effects and molecular fragmentation[34] also contribute to the final uncertainty on the mole fraction determination. Considering all these aspects, the uncertainty of the quantified mole fractions is in the order of 15% for the main species (fuels, oxygen, and main combustion products) and about 30% for directly calibrated intermediate species; the latter increasing by a factor of 2-3 when the calibration factor is obtained indirectly through convolution[31] or the relative ionization cross sections (RICS) method.[35] An overview of the

Table 1: Inlet mole fractions and conditions of the investigated flames [p = 60 Torr (80 mbar) and inlet temperatures T_{fuel} = 333.15 K and $T_{oxidizer}$ = 303.15 K].

	$Flame_{CP}$	$Flame_{CPME}$
Fuel side		
C_5H_8	0.12	0.12
CH_4	-	0.10
Ar	0.88	0.78
Oxidizer side		
O_2	0.36	0.33
Ar	0.64	0.67
Strain rate [1/s]	60	60
Stoichiometric mixture fraction	0.33	0.26
Flame T_{eq} [K]*	2740	2729
Inlet carbon mass fraction	0.17	0.21
C/H ratio	7.44	6.13

* These values refer to simulations performed with the thermochemistry data of the Gueniche model, for CRECK the computed equilibrium temperatures are 2730 and 2719 K for $Flame_{CP}$ and $Flame_{CPME}$, respectively.

calibration strategies that were applied to the different species and other relevant related information is available in Table S1.

The main goal of this work is the assessment of the importance of the simplest ring-enlargement reactions (Eqs. 3-5). To this end, relative comparisons of the experimental values appear to be more meaningful. This leads to the advantage that many sources of error are canceled out and the uncertainty in the relative comparisons reduces to 10% also for intermediates. For the presented measurements, burner scans for main species were performed with a nominal electron energy of 17 eV, while intermediate species were measured at 9.5, 10.25, and 12 eV for a more reliable comparison and evaluation of possible fragmentation effects.

Table 1 summarizes the flame conditions: $Flame_{CP}$ consists of a counterflow cyclopentene-oxygen flame diluted with argon, while $Flame_{CPME}$ also includes CH_4 on the fuel side. Following the strategy presented in a previous work,[33] the main structural quantities of the two counterflow flames, that are investigated here, were kept in a comparable range. Specifically, the low strain rate allows for a sufficient flame thickness and therefore a significant number of sampling points; the stoichiometric mixture fraction and the equilibrium temperature were kept similar by adjusting the oxygen concentration to compensate for the methane addition. The slight difference in these last two quantities between the two flames, which in any case does not affect the conclusions of this work, could have been further reduced by adding a limited amount of methane to the base flame of cyclopentene. However, it was decided to adjust more significantly the carbon inlet mass flow rate to better assess the effect of methane addition.

All gas flows used in these experiments were introduced with MKS mass flow controllers with a precision of 0.5% on the full scale, while the fuel was supplied through a Quantim coriolis mass flow controller (BROOKS) and vaporized in a BRONKHORST unit. Considering the nozzle geometry, which is provided in the Supplementary Material (see Fig. S1), and the necessity to leave a minimal gap between the fragile quartz probe and the burner outlet, sampling measurements were performed for a global length of 11 mm. A step size of 0.2 mm in the flame "pyrolysis" region and 0.25 mm on the oxidizer side was chosen.

3.Theoretical calculations and kinetic modeling

3.1 Hydrogen abstraction reactions from C_5H_6

Given the crucial role of C_5H_5 concerning PAH formation in cyclopentene flames, important formation pathways for this radical were revisited in this work. The addition and abstraction reactions of atomic hydrogen to and from cyclopentadiene (C_5H_6) have been extensively described in a recent publication.[36] We extended this earlier work to also cover H-abstraction reactions via four other important radicals: CH_3, $O(^3P)$, OH, and HO_2.

The electronic energies of reactants, reactant complexes, transition states, product complexes, and products were calculated at the CCSD(T)/cc-pVDZ and CCSD(T)/cc-pVTZ levels based on optimized structures (see next). The electronic energies were then extrapolated to the complete basis set (CBS) limit as proposed by Truhlar:[37]

$$E_{CBS} = \frac{3^\alpha}{3^\alpha - 2^\alpha} E_{X=3}^{HF} - \frac{2^\alpha}{3^\alpha - 2^\alpha} E_{X=2}^{HF} + \frac{3^\beta}{3^\beta - 2^\beta} E_{X=3}^{cor} - \frac{2^\beta}{3^\beta - 2^\beta} E_{X=2}^{cor} \quad (6)$$

where E^{HF} and E^{cor} are the Hartree-Fock (HF) and the correlation energies, respectively. For the CCSD(T) method, α = 3.4 and β = 2.4; X = 2 and 3 represent the cc-pVDZ and cc-pVTZ basis sets. The multi-reference characteristic parameter, T1 diagnostic, obtained from CCSD(T)/cc-pVTZ calculations, is provided in the Supplementary Material and was found to be smaller than the thresholds (0.02 and 0.045 for closed-shell and open-shell species, respectively) for all the species. In particular, the T1 diagnostic of the transition state of hydrogen abstraction by $O(^3P)$ is 0.42, which is smaller than the threshold of 0.045 for an open-shell system.[38] A previous study of the hydrogen abstraction from toluene by $O(^3P)$ from Pelucchi et al.[39] indicated that the single state single reference and multistate multireference calculations were in good agreement within 0.1 kcal/mol. This indicated that the systems considered in this study were weakly correlated and the single-reference method was reliable to obtain energies of reactions.

The geometries and frequency analysis of the stationary points on the potential energy surface (PES) along the reaction pathways of CH_3, $O(^3P)$, OH, and HO_2 were optimized via density functional theory (DFT) with the hybrid exchange-correlation functional M06-2X and the 6-311+G(d,p) basis as in Mao et al.[36] To account for the anharmonicity, the normal mode vibrational frequencies were obtained based on the harmonic approximation and the zero-point

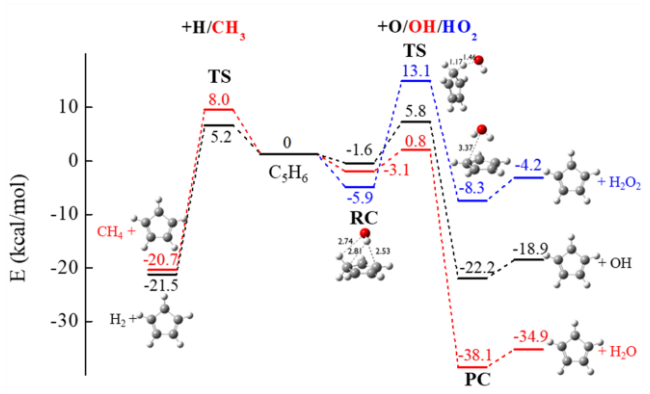

Fig. 1: Zero-point energies corrected potential energy surface (PES) of hydrogen abstraction from the CH_2 group of C_5H_6 by $H/CH_3/O/OH/HO_2$ at the CCSD(T)-CBS//M06-2X/6-311+G(d,p) level of theory [kcal/mol].

energies (ZPEs) were obtained by scaling the M06-2X/6-311+G(d,p) results by 0.97.[40, 41]

All quantum chemistry calculations were carried out using the Gaussian 09 program.[42]

Figure 1 shows the PES of hydrogen abstraction reactions from site 1 (which refers to the CH_2 part of C_5H_6, a detailed notation is given in Fig. S10) of C_5H_6 by CH_3, $O(^3P)$, OH, HO_2, and H forming cyclopentadienyl. The H + C_5H_6 reaction results are taken from the work of Mao et al.[36] Prior to reach the transition state, a reactant complex (RC) forms via hydrogen bonding between the H atom in C_5H_6 and the O atom of the $O(^3P)$, OH, and HO_2 radicals. In the same way, a product complex (PC) forms on the product end. The intrinsic reaction coordinate (IRC) analysis was performed at the same level of geometry optimization to confirm that the transition state (TS) connects the corresponding reactants and products on both sides on the PES. The RCs and PCs were obtained by optimizing the structures at the two ends of the IRC curve with over 150 intervals of the forward and backward for corresponding TSs.

As expected, the barrier height for hydrogen abstraction by the HO_2 radical is the highest, followed by the barrier for the CH_3+C_5H_6 reaction. The energy barriers for the hydrogen abstraction by H radical and O radical are at comparable heights. The hydrogen abstraction reaction by OH has the lowest barrier. These trends are consistent with the results for hydrogen abstractions from methyl groups of acetate and propanoate.[43, 44] The PES for the hydrogen abstraction from C_5H_6 from sites 2 and 3 (which refer to the one next to the CH_2 group and to the one furthest away, respectively) are attached in the Supplementary Material. It was found that the hydrogen abstraction from site 1 is preferred over those at site 2 and 3 for all the five radicals as the barrier height is at least 10 kcal/mol lower; with the exception of OH reactions exhibiting a difference of about 5 kcal/mol. Moreover, the five hydrogen abstraction reactions discussed here are all exothermic for site 1, while computations performed for abstractions from sites 2 and 3 show that they are endothermic except for the reaction with OH radical.

The rate constants for the hydrogen abstraction reactions by CH_3 radicals were calculated using the conventional transition state theory (cTST) as it was done for the H radical.[36] For the hydrogen abstraction reaction by O, OH, and HO_2, the barrierless entrance channel to form a RC features a potential that is long-range in nature and weakly depends on the form of the reaction coordinate. Therefore, the entrance reaction forming the RC was modeled based on the phase space theory (PST).[45] Specifically, the PST was approximated by a simplified isotropic interaction, $V(R) = C_6/R^6$, where C_6 can be estimated by $C_6 = 1.5\ \alpha_1\alpha_2E_1E_2/(E_1 + E_2)$, where α_i and E_i are the polarizability and ionization energy of species *i*, and *i* = 1,2 represents C_5H_6 and $O/OH/HO_2$, respectively. Therefore, the estimated C_6 is 48.7, 73.8, and 154.4 $Bohr^3Hartree$ for C_5H_5 + O, C_5H_5 + OH and C_5H_5 + HO_2, respectively. The temperature and pressure dependent reaction rates were obtained by solving the RRKM/master equation with the kinetic code MESS[46] in the temperature range of 500-2500 K and the pressure range of 0.01-100 atm (see the Supplementary Material for input files). The low-frequency modes of the internal rotors of the transition states of the hydrogen abstraction by OH and HO_2 were treated as 1-D hindered rotors[43, 44] with hindrance potentials computed at the level of M06-2X/6-311+G(d,p). For other vibrational models, harmonic oscillator assumptions were employed to evaluate the densities of states of species. The asymmetric 1-D Eckart tunneling corrections[47] were included to compensate for the tunneling effects. For the collisional model used in the master equation, interaction between the reactant and the bath gas Ar was modeled by the Lennard-Jones (L-J) potential. For Ar, σ = 3.47 Å, ε = 79.23 cm^{-1} and for C_5H_5, σ = 5.78 Å, ε = 273.8 cm^{-1} were used as approximations. The collisional energy transfer function was represented by a single-parameter exponential down model with $\Delta E = 400\times(T/300)^{0.7}\ cm^{-1}$, which has been widely used for C_5H_6 and aromatics.[48-50] The rate constants of the investigated reactions are fitted to a single Arrhenius equation as a function of temperature

$$k = AT^n e^{(-E_a/RT)}, \quad (7)$$

where *A* is the pre-exponential factor in the unit $cm^3mol^{-1}s^{-1}$ or s^{-1}, *T* is the temperature in Kelvin, *n* is the temperature exponent, E_a is the activation energy in cal/mol. Table 2 provides the high-pressure limit (HPL) rate constants of the hydrogen abstraction reactions.

The rate constant for the H abstraction from C_5H_6 by H atom at site 1 has been compared against previous studies based on theoretical calculations from Moskaleva and Lin[50] and those based on analogy rules from Emdee et al.,[51] Zhong and Bozzelli,[52] Djokic et al.,[53] and Narayanaswamy et al.[54] It was found that the rate constant from the present study lies among the reported results as shown in Fig. S11. Because the entrance well of the reactant complex is quite low, the effect of the pressure on the reaction rate is only relevant at low temperatures. Specifically, for the hydrogen abstraction by OH (Fig. 2), a significant deviation of the rate constant at different pressures occurs at temperatures lower than 250 K. In addition,

Table 2: Rate coefficients for hydrogen abstraction reactions.

Reaction		A [$cm^3mol^{-1}s^{-1}$]	n	E_a [cal/mol]	Fitting T [K]	MAE*	
$C_5H_6 + H \rightleftarrows C_5H_5 + H_2$	HPL	1.42E+07	2.091	3300.00	500-2500	1.08%	13.6%
$C_5H_6 + CH_3 \rightleftarrows C_5H_5 + CH_4$	HPL	2.78E+00	3.73	4701.60	500-2500	0.97%	1.89%
$C_5H_6 + O(^3P) \rightleftarrows C_5H_5 + OH$	HPL	6.20E+06	2.12	4855.20	500-2500	2.29%	4.89%
$C_5H_6 + OH \rightleftarrows C_5H_5 + H_2O$	HPL	8.87E+04	0.02	-1133.90	500-2500	2.44%	5.29%
$C_5H_6+HO_2 \rightleftarrows C_5H_5 + H_2O_2$	HPL	1.29E-04	4.65	6909.43	500-2500	15.65%	52.81%

* MAE: measure on the fitting error on the Arrhenius fit, MAE = mean(abs((theory-fit)/theory))

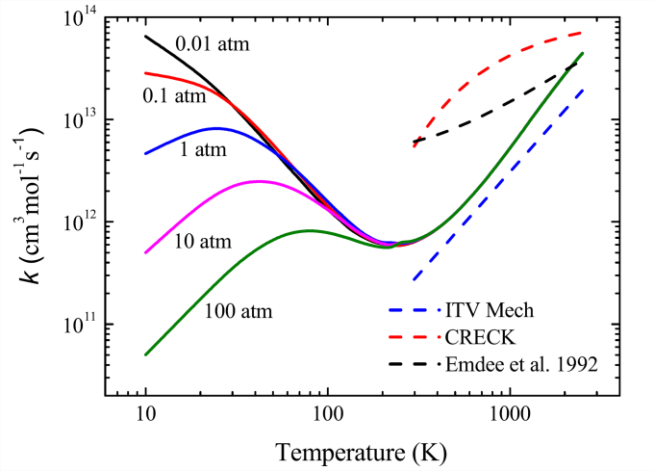

Fig. 2: Pressure- and temperature-dependent rate coefficient for H-abstraction from C_5H_6 by OH radicals at site 1 together with the HPL rate coefficients in comparison with the available literature.[43-45] Dashed lines: previous works; solid lines: this study.

particularly for the high-temperature region, Fig. 2 shows that our new results (solid lines) lie among the values computed in previous works[51, 54, 55] (dashed lines).

3.2 Modeling of the ring-enlargement reactions

Numerical simulations were performed with two different chemical mechanisms to elucidate the importance of ring-enlargement reactions. The first mechanism, here referred to as "Gueniche", consists of 2173 reactions and 175 species.[25] Its sub-sections, which comprise C_3 and C_4 hydrocarbons as well as benzene and toluene, were previously tested against speciation measurements in flames, jet-stirred reactors, and laminar flow reactors. This mechanism was chosen because it was specifically updated to address methane-doped cyclopentene flames, and therefore includes a detailed methylcyclopentene subset. A more recent mechanism was developed by Herbinet et al.,[23] which could not be applied in this work because it was specifically developed for pyrolysis conditions.[56]

The second mechanism, here referenced as "CRECK", was developed by Pejpichestakul and co-authors.[55] It consists of 7862 reactions and 250 species including a cyclopentene subset, which was added to model cyclohexane flames.[57] This mechanism was

Table 3: Ring-enlargement routes involving C_5H_5 included in the two mechanisms. Different reactants or products featuring the same number of carbon atoms are conceivable, which explains the generality of the notation.

Reaction	CRECK	Gueniche	Products
$C_5H_5 + C_1 \rightarrow C_6$ (*)	✓	✓	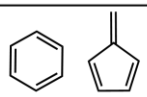
$C_5H_5 + C_2 \rightarrow C_7$		✓	
$C_5H_5 + C_3 \rightarrow C_8$	✓		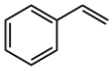

* different pathways are possible to obtain the same product

tested against a cyclopentene premixed flame. The decision to incorporate it into our analysis was motivated by the very good performance in predicting the effect of methane addition in the comparative study of Baroncelli et al.[33] In that work, naphthalene decomposition reactions were identified to be responsible for the formation of indene and styrene, thus making this mechanism a very good candidate to test the effect of molecular growth vs. decomposition pathways for the formation of some small aromatic species.

The mole fraction profiles as a function of the distance from the fuel outlet were computed with the code *FlameMaster*,[58] which has been routinely used to simulate counterflow flames.[33, 59, 60]

Comparing the modeling with the experimental results revealed the opportunity to assess the importance of the ring-enlargement reactions in high-temperature flame environments. A summary of the routes initially present in the two mechanisms is provided in Table 3. Both mechanisms describe RERs with some distinct differences: the CRECK model includes the formation of fulvene and benzene from methylcyclopentadiene (MCPT) as two one-step reactions, while in the Gueniche model the formation of benzene passes through the sequence represented in Fig. 3.

The formation of C_7H_7 radicals (benzyl) via a global reaction $C_5H_5 + C_2H_2 \rightarrow C_7H_7$ was considered only in the Gueniche mechanism. As mentioned in Section 1, the possible formation of toluene via

acetylene addition to C_5H_5 was investigated by Cavallotti and co-authors[17, 19] in studies which were published after the Gueniche model had been developed. Cavalotti and coworkers concluded that a direct formation C_7H_7 would be hampered by high energetic barriers and that benzyl production would occur via isomerization of the cycloheptatrienyl radical.

In the CRECK mechanism, the role of cyclopentadienyl in the formation of C_8 substituted aromatics is included via the reaction $C_5H_5 + C_3H_3 \rightarrow C_8H_8$. Simulating the flames of this work, this reaction emerged as the main formation pathway for styrene, as will be discussed below.

Without altering the main goal of this work, which is to analyze the importance of RERs of the cyclopentadienyl radical for PAH formation, we decided to:

1. incorporate the new theoretical calculation results previously described (Section 3.1) into the two mechanisms;
2. substitute the one-step reaction channel from methylcyclopentadiene to benzene with the sequence shown in Fig. 3 in the CRECK model;
3. include a new reaction to produce C_8H_{10} (ethylbenzene), C_5H_5 + a-$C_3H_5 \rightarrow C_8H_{10}$, which connects the production of ethylbenzene to the C_5H_5 radical. Because no rate constant is available for the proposed reaction, it was decided to use the same rate as for the reaction responsible for styrene production. A more detailed explanation which motivates this choice is given below in Section 4.4.

These changes of the CRECK mechanism just marginally influenced the prediction of the ongoing chemistry at the early stages of the fuel decomposition. The changes concerning benzene and ethylbenzene must be considered as a pure explorative test. In the following sections, this version of CRECK will be referred as "CRECK$_{rev}$". A concise overview of the changes to the original model can be found in Table S2 of the Supplementary Material and the entire mechanism, i.e. kinetic set, thermodynamic and transport data is provided as Supplementary Material.

The goal of the numerical simulations is to assess the sensitivity of the newly calculated rates and the newly included reactions for predicting the concentration of aromatic species. The comprehensive validation of the newly assembled mechanisms is outside the scope of this work. Nevertheless, the Supplementary Material includes some comparison against laminar burning velocity and plug-flow reactor measurements.[61, 62] Concerning the ring-enlargement reactions, it is discussed below that the incorporation of the aromatic formation pathways as described above can explain some experimental trends. However, more stringent tests are certainly desirable.

Concerning the Gueniche mechanism, the rate of the $C_5H_5 + C_2H_2 \rightarrow C_7H_7$ reaction is extremely fast that it affects the formation of all aromatic species. This fact made it difficult, and probably meaningless, to perform the same kind of assessment as it was done for the CRECK mechanism. However, the newly calculated reaction rates, which were introduced in Section 3.1, were also tested for this model, but their effect was not as impactful as they were for the CRECK mechanism. The mole fraction profiles computed with this version of the Gueniche model can be found in the Supplementary Material.

4. Results and discussion

4.1 First inspection of the mass spectrum

An analysis of the mass spectra, like the one shown in Fig. 4, which was recorded after sampling from Flame$_{CP}$ at 8 mm from the fuel outlet, and the comparison with literature data can already reveal important information about ring-enlargement reactions. A remarkable tendency of the fuel to form PAHs can be observed, as evidenced in mass spectral signal for species beyond mass-to-charge (m/z) ratios of 202 ($C_{16}H_{10}$).

Following the approach of Hansen et al.,[63] repetitive mass growth sequences can be identified in the mass spectra that lead to the formation of PAHs. As an example, starting from benzene (m/z=78), signal blocks in which the peaks of the species are separated by 24

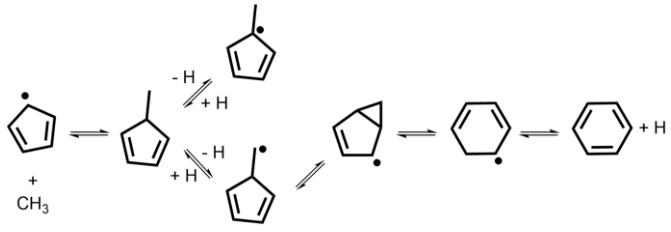

Fig. 3: Reaction sequence included in the Gueniche model to account for the formation of benzene from the cyclopentadienyl radical. This figure is adapted from Herbinet et al.,[23] where it is reference as Figure 7.

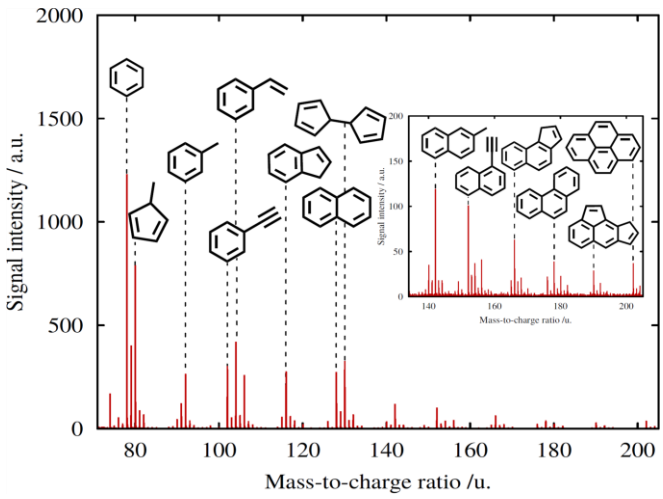

Fig. 4: Mass spectrum obtained from Flame$_{CP}$ at 8 mm from the fuel outlet. The molecular structure of the most probable species for the given m/z ratio is provided. However, contributions from other isomeric forms cannot be ruled out.

mass units are likely to reveal the presence of hydrogen-abstraction-acetylene-addition (HACA) mechanisms. Whereas, a separation of 14 mass units might imply the occurrence of hydrogen-abstraction-methyl-addition (HAMA) sequences. In this section, we will not repeat the full analysis which has been extensively performed for C_4 and C_5 fuels by Hansen et al.[63] and Ruwe et al.,[64] but we will limit our observations to the more relevant aspects which concern these specific measurements.

As already mentioned, the cyclopentadienyl radical is likely to show a prominent role in the soot precursor formation. However, the extent of this link has not been sufficiently clarified yet, which is partly due to the scarcity of experimental data. In Fig. 4, a significant peak is observed at *m/z*=80 which corresponds to C_6H_8 (also visible in $Flame_{CPME}$). While the type of experimental technique employed in this work does not allow for isomer-resolved measurements, most likely molecular structures are cyclohexadiene and methylcyclopentadiene, both of which have been detected in pyrolysis and flame experiments before.[23, 26, 61] Considering the nature of the two fuels and the experimental results which will be presented in the following of this work, assigning this signal to methylcyclopentadiene seems to be a reasonable choice. Supportive evidence in favor of this hypothesis is presented below (Section 4.3), but the contribution of other isomers is certainly expected. Similar arguments can be used to assign mass *m/z*=82 to the most likely isomers methylcyclopentene and cyclohexene.

Furthermore, the signal at *m/z*=104, which most likely corresponds to styrene, is more pronounced than that corresponding to phenylacetylene (C_8H_6) at *m/z*=102. On a first glance, this result might be surprising as many mass growth sequences do not include *m/z*=104 in their steps. Hansen et al.[63] and Ruwe et al.[64] speculated on a possible fast dehydrogenation of C_8H_{10}, which would be formed from benzene by two consecutive HAMA sequences. Other possible reasons could lie in alternative formation pathways of styrene that occur via decomposition of naphthalene or that include a direct contribution of the cyclopentadienyl radical via $C_5H_5 + C_3H_3 \rightarrow C_8H_8$.

A strong indication of the significant role that C_5H_5 might play is given by the pronounced signal corresponding to $C_{10}H_{10}$ (*m/z*=130), which most likely comes from the recombination of two C_5H_5 molecules. A comparison of Fig. 4 with the spectrum measured by Ruwe et al.[64] shows a significantly different peak height ratio between $C_{10}H_{10}$ and $C_{10}H_8$. In our study the peak of the $C_{10}H_{10}$ signal is higher than that measured for $C_{10}H_8$, whereas in Ruwe et al. the ratio $C_{10}H_{10}/C_{10}H_8$ was about 1:3. This remarkable difference suggests that for different C_5 fuels, some molecular growth sequences might play different roles.

A qualitative analysis of the mass spectra shows that signal intensities are similar between the cyclopentene and the methane-doped flame (see Fig. S2). While this might be surprising at first, a more detailed analysis reveals intriguing chemical differences. In the following, we base our analysis on the quantification of the detected intermediates and on the relative comparison between the two flames.

4.2 Initial fuel decomposition steps

The correct identification of the initial fuel destruction steps is a prerequisite for chemical mechanisms to correctly assess the importance of RERs. Therefore, a discussion about these early decomposition steps is presented in the following sections.

4.2.1 Small hydrocarbons

As several comparative studies have demonstrated,[64-66] fuel decomposition steps play a pivotal role in providing the stable intermediates and radical pool necessary to initiate molecular growth routes. These reactions depend on the molecular fuel structure and are generally organized in reaction classes.

In this work, the mole fraction profiles of the reactants and the major combustion products were quantified and compared to the results of simulations for each of the two mechanisms presented in Section 3.2. Results are reported in Fig. S3. It should be noted that

(a) Gueniche (b) CRECK

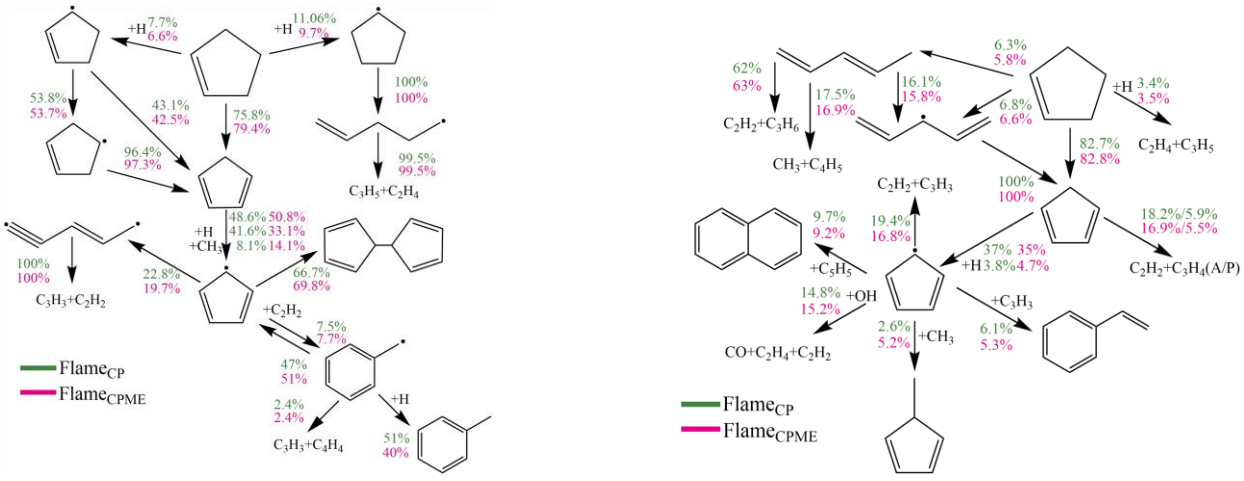

Fig. 5: Predicted fuel decomposition pathways according to the two chemical mechanisms.

the maximum deviation between the experimental values and the simulations of these main species falls inside the given experimental uncertainty. The overall good agreement between the simulations and the experimental data makes it possible to perform a meaningful reaction flux analysis of the fuel decomposition. This analysis was performed for both mechanisms and is presented in Fig. 5.

According to Gueniche (Fig. 5a), the dominant fuel consumption channel is the molecular dehydrogenation, which forms hydrogen and cyclopentadiene. The addition of an H atom to form cyclopentyl is responsible for 11% of the fuel consumption. The third decomposition channel is the formation of 2-cyclopentenyl, which occurs mostly via hydrogen abstraction by H radical, and is followed by a quick isomerization into 3-cyclopentenyl. Besides the cyclopentyl, whose isomerization into 1-penten-5-yl leads to the production of ethylene (C_2H_4) and allene (a-C_3H_4) via β-scission, the first and the third consumption channels directly or indirectly lead to the production of cyclopentadiene. Under these conditions, hydrogen abstraction reactions entirely convert cyclopentadiene into the cyclopentadienyl radical, which can in turn isomerize into pent-1-yne-3-ene, recombine into bicyclopentadienyl, or take part into molecular growth pathways to form benzyl radicals. As stated in Section 1, these reactions are of key importance for formation of PAHs and will be discussed in the following.

The fuel decomposition scheme according to CRECK is presented in Fig. 5b. It shows the importance of cyclopentadiene as the main consumption product (more than 80% of the fuel is consumed via this route). Compared to Gueniche, the main differences consist in the missing H atom addition to the C=C double bond in CRECK, while in Gueniche this reaction leads to cyclopentyl and subsequently to 1-penten-5-yl. Instead, CRECK includes direct cyclopentene isomerization into 1,3-pentadiene, which is followed by thermal cleavage into C_1-C_4 compounds. As in the Gueniche mechanism, the cyclopentadienyl radical obtained via H abstraction from cyclopentadiene can either participate in the formation of aromatics species or form smaller C_2 and C_3 species. Overall, the CRECK mechanism differs from the Gueniche for the larger presence of global reactions replacing β–scission or decomposition reactions of the fuel radical.

This first inspection of the initial reaction steps in the fuel consumption suggests that, among the stable intermediates, cyclopentadiene and C_2-C_3 hydrocarbons are expected to be produced in large amounts. The comparison between the measured and computed mole fraction profiles of these species is given in Fig. 6. As a general note, the species profiles showed in the upcoming sections refer to $Flame_{CP}$, while just a relative comparison is provided for $Flame_{CPME}$. The full set of profiles for $Flame_{CP}$ and $Flame_{CPME}$ is provided in the Supplementary Material. The amount of C_5H_6, C_2H_2, C_2H_4 predicted by the two models is quite similar. In fact, these species appear in the early decomposition stages of the fuel in both models. Here C_5H_6 was calibrated as cyclopentadiene, although 1-pentene-3-yne, was identified before in a cyclopentene laminar premixed flame.[29] Overall the agreement between the experimental data and the numerical simulations is quite satisfactory as the model predictions fall inside the experimental uncertainty (see Sect. 2 and Table S1). Consistent with previous works,[30, 67, 68] the experimental profiles appear slightly broader than those computed with the two models which might be attributable to the presence of the intrusive quartz probe. But because of the consistent underprediction of the oxygen side, uncertainties in the kinetic description of the oxidation reactions cannot be ruled out either.

Differently from the C_2 and C_5 intermediates, the amount of C_3H_4 isomers and propene (C_3H_6) is significantly underestimated by the Gueniche model, while the prediction of the CRECK model falls inside the experimental uncertainty. A detailed analysis of the reasons for this difference can be found in Sec. 4.2.2. It should be mentioned that C_3H_4 was calibrated as propyne based on the results of the two models which indicate propyne (p−C_3H_4) as the most abundant isomer.

4.2.2 Consequences upon methane addition

As shown in Fig. 5, both models do not predict substantial changes in the fuel consumption channels caused by methane addition. The most noteworthy effect was the replacement of the H radical with CH_3 in H abstraction reactions. However, to analyze the effect of methane addition in more detail, Fig. 7 presents the comparison of the reaction rates for the most important C_5H_8 consumption reactions between the two flames. In presence of methane, the rate of these reactions decreases, which therefore hinders the production of intermediates that are directly correlated to cyclopentene decomposition. The reason for this change is twofold and related to thermal and chemical effects. First, even if the temperature profile of the two flames are quite similar, $Flame_{CPME}$ is about 40 K colder than $Flame_{CP}$ in the region where the fuel decomposition reaches the peak. This effect is quite important for the fuel dehydrogenation

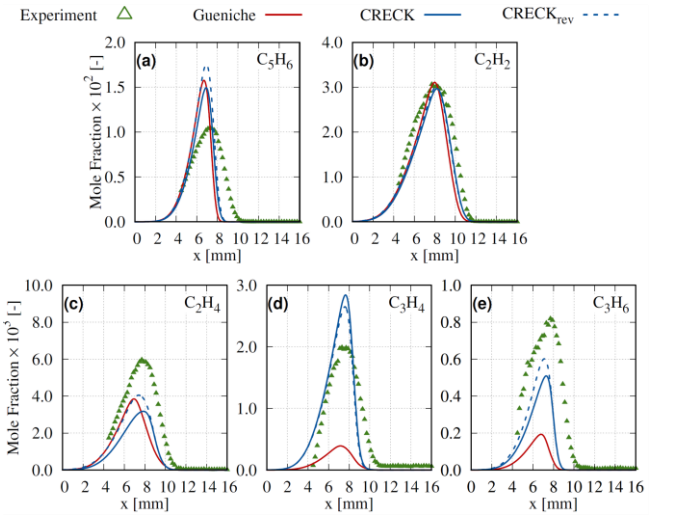

Fig. 6: Comparison between measured (symbols) and computed (lines) stable intermediates which are formed in the early stages of the fuel decomposition. Here results are provided for $Flame_{CP}$, the axial coordinate *x* represents the distance from the fuel outlet.

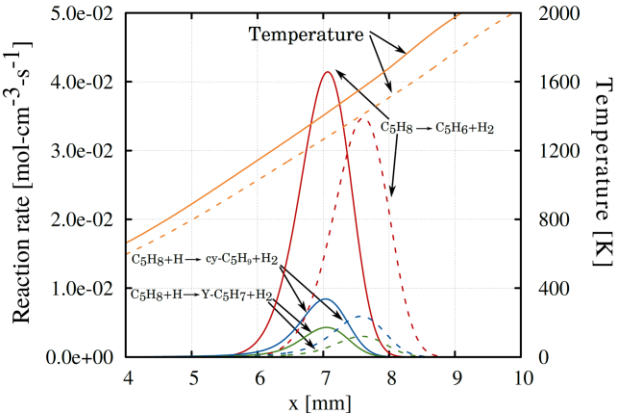

Fig. 7: Left axis: reaction rate profile for the three most important C_5H_8 consumption reactions in the Gueniche model (computations with the CRECK model follow the same trends); right axis: temperature profile. Solid lines correspond to $Flame_{CP}$ and dashed lines to $Flame_{CPME}$. Variables are shown as a function of the distance from the fuel outlet.

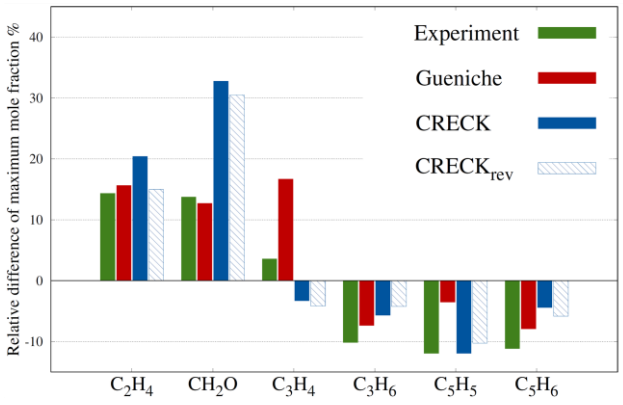

Fig. 8: Relative differences of the mole fraction maxima between $Flame_{CP}$ and $Flame_{CPME}$ (%)

reaction $C_5H_8 \rightleftarrows C_5H_6 + H_2$ which constitutes the main fuel decomposition route. Second, the competition for the H radical caused by the reaction $CH_4 + H \rightleftarrows CH_3 + H_2$ weakens some other important pathways such as $C_5H_6 + H \rightleftarrows C_5H_5 + H_2$.

This reduced availability of H is not compensated by a larger amount of methyl radicals because as the PES depicted in Fig. 1 shows, CH_3 is not as active as H in abstracting an H atom from C_5H_6. This effect explains the more pronounced decrease of the C_5H_5 concentration compared to the observed decrease of the C_5H_6 amount. In Sections 4.3 and 4.4 it will be shown that this aspect is of fundamental importance to explain the observed trends in several aromatic species.

In Fig. 8, relative increments/decrements in the maximum mole fraction with respect to $Flame_{CPME}$ are depicted for several intermediates which include C_5H_5 and C_5H_6 together with some small hydrocarbons. In presence of methane, the concentrations of ethylene and formaldehyde (CH_2O) increase, which is expected, given the participation of methyl radical in formation pathways for these species. Despite the different predicted amount of propene (see Fig.6), both mechanisms show a decrease in the mole fraction of C_3H_6 for $Flame_{CPME}$. For C_3H_4, the Gueniche mechanism predicts a strong increase in the global amounts of both allene and propyne. In contrast, the CRECK mechanism shows just a slight reduction which is closer to the observed experimental result where just a small increase is observed. In the remaining part of the section, a deeper inspection of the reasons causing the differences between the two models regarding C_3 hydrocarbons is performed. These species can in fact play a paramount role in providing the pool of propargyl radicals, which in many cases is the fundamental molecule to form benzene.[6, 69, 70]

To assist the analysis, Figures 9-10 depict integrated consumption and production rates for these C_3 species. It can be seen that, despite their differences, both models relate the formation of

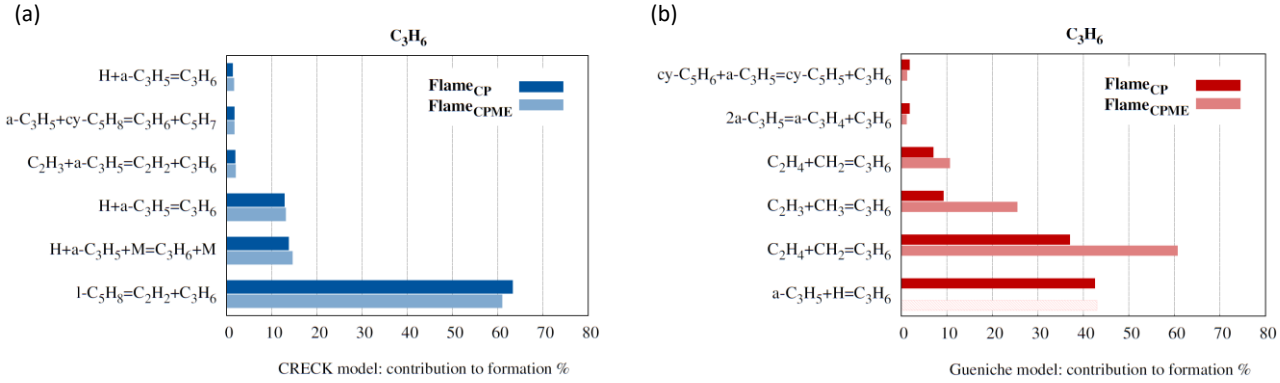

Fig. 9: Integrated relative production rate for propene. Contribution above 2% were considered. The non-solid bar in panel (b indicates that the corresponding reaction becomes a consumption reaction.

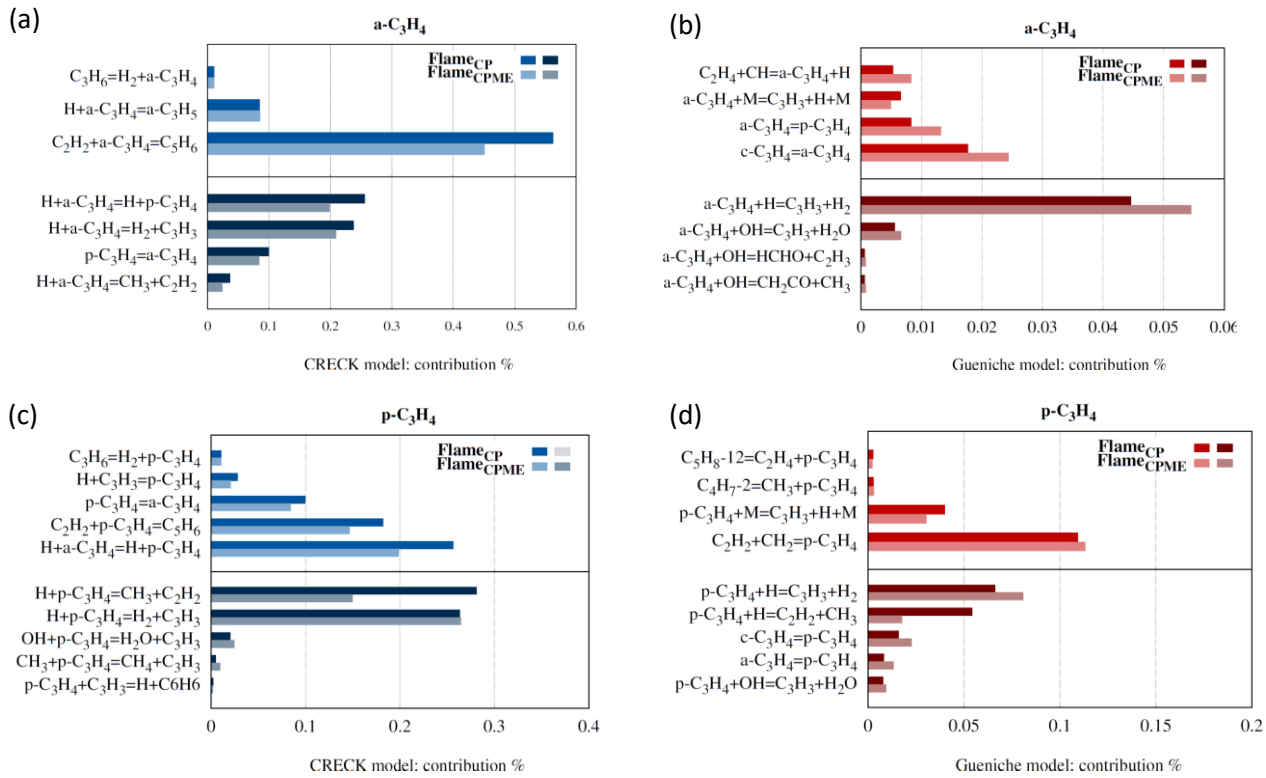

Fig. 10: Integrated production and consumption rate for propyne (p-C_3H_4) and allene (a-C_3H_4). Contributions above 2% were considered. The upper and lower parts of the four panels correspond to production and consumption reactions, respectively.

propene to the early decomposition stages of the fuel where the allyl radical (a-C_3H_5) is produced. In addition, the CRECK model includes the contribution of the decomposition of l-C_5H_8 which is missing in the Gueniche mechanism. When methane is added, a combined effect which involves a slower C_5H_8 consumption and the equilibrium shift of the main production reaction (see the non-solid bar in Fig. 9b) causes a decrease in the propene amount. As expected, for the CRECK model the most important production pathway is the decomposition of the fuel isomer, which is faster in the $Flame_{CP}$. Overall, despite the differences between the two mechanisms, the production of C_3H_6 in $Flame_{CP}$ is strongly connected to the reactivity of C_5H_8 which is hampered by the methane addition, thus explaining this trend which is confirmed by the experiments.

Concerning C_3H_4, its measured amount is essentially identical in both flames, while the two models predict different trends. For the sake of clarity, Figure 10 shows the integrated values of the reactions which contribute the most to the formation and consumption of allene and propyne, and not their relative contribution. This is necessary to better clarify the role of the consumption pathways. In the CRECK model the decrease of C_3H_4 mole fraction for $Flame_{CPME}$ is attributable to allene, while propyne does not show an appreciable change. Panel (a) of Fig. 10 depicts the most significant reactions for allene, whose amount diminishes because of the decrease in C_5H_6. Because propyne is mainly formed from isomerization of allene and decomposition of cyclopentene, it appears clearly how its absolute production would decrease upon addition of methane. Also, allene consumption is reduced in the $Flame_{CPME}$, which results in an unchanged mole fraction. In the Gueniche model, no fuel-specific decomposition pathway exists to form C_3H_4 isomers. Different from the CRECK, in the Gueniche model allene is produced from p-C_3H_4 isomerization. In fact, propyne is mostly produced via $C_2H_2 + CH_2 \rightleftarrows$ p-C_3H_4, but also $CH_3 + H$ (+M) $\rightleftarrows$ p-C_3H_4 (+M) plays a significant role and is responsible for the reduced absolute production of this species. Also, in this case, the reduced consumption through p-$C_3H_4 + H \rightleftarrows C_2H_2 + CH_3$ determines its increase and consequently affects also the allene amount.

To conclude, both models have demonstrated a quite good prediction of the effects of methane addition on cyclopentene. It was therefore decided to include their predictions as supportive means to assess the role of RERs in aromatics formation and growth.

The following section presents the comparison between the experimentally and numerically determined mole fraction profiles of some selected species in the two flames. Specifically, the possibility of ring enlargement via $C_5H_5+C_1$ and $C_5H_5+C_2/C_3$ species are explored and naphthalene formation is discussed.

4.3 First ring enlargement route: $C_5H_5+CH_3 \rightarrow C_6H_6$ and analogous

In Sections 1 and 3.2, two slightly different versions of this route have been already introduced. The first version involves the formation of

the methylcyclopentadienyl radical, H loss to form fulvene and isomerization into benzene; the second one passes through the cyclization of the C_6H_7 radical (see Fig. 3) followed by H loss. This ring-enlargement path represents the smaller, but chemically analogous, version of the reaction sequence investigated by Zhao et al.[16] In the case of Zhao et al., the authors were able to identify methylindenyl and methylindene isomers to proof the existence of a pathway which, through methyl radical addition, converts indene into naphthalene. Different from the indenyl radical, which is relatively stable, cyclopentadienyl might be rather unstable at high temperatures as it tends to decompose into acetylene and propargyl (Eq. 1).

To our knowledge, a direct measurement of the radicals involved in this transition from C_5 to C_6 hydrocarbons has not yet been performed. However, the difficulty to detect the presence of such species to assess the importance of these enlargement reactions in forming C_6 aromatics in flame environments, could be circumvented by the identification of other stable intermediates. In this section we intend to contribute to this assessment.

Figures 11a-b illustrate the results for C_6H_6 and C_6H_8 for the two flames. The overall agreement between the models and the simulations appears quite good. As stated in Section 4.1 the experimentally obtained signal corresponding to C_6H_8 was calibrated as MCPT. In both mechanisms this species is produced via the reaction $C_5H_5 + CH_3 \rightleftarrows$ MCPT. By comparing the experimental mole fraction profile with those obtained from the numerical simulations, we noticed that, although the onset of the C_6H_8 is correctly predicted by the models, the peak of the experimental results is shifted by approximately 2 mm towards the oxidizer side. This effect, which is not observed for benzene, might reveal some missing pathways in the chemical mechanisms. In fact, near the stagnation plane, the higher flame temperature could favor the recombination of allyl and propargyl radicals to form cyclohexadiene, which would then contribute to the C_6H_8 signal. Another aspect that should also be considered is the uncertainty on the given reaction rates, a sensitivity analysis performed by multiplying the pre-exponential term by a factor of two shows that in this case the amount of MCPT would increase by 22%.

In Fig. 11b the decrease of the predicted MCPT mole fraction for the CRECK$_{rev}$, is due to the inclusion of the new benzene formation pathway (Section 3.2), which consumes C_5H_5, and to the newly applied reaction rates (Section 3.1). Although the agreement with the experimental mole fraction is reduced, the absence of reactions which can lead to cyclohexadiene, and thereby also contribute to the C_6H_8 signal, could well explain this discrepancy.

Further insights into possible formation pathways can be provided by an additional comparison between relative changes in the maximum mole fraction in Flame$_{CP}$ and Flame$_{CPME}$. In Figure 11c, it can be observed that upon addition of methane, the measured C_6H_6 and C_6H_8 mole fractions, increase by 20% and 30%, respectively. This result provides the experimental confirmation that not only benzene, but also other species which are intrinsically correlated to

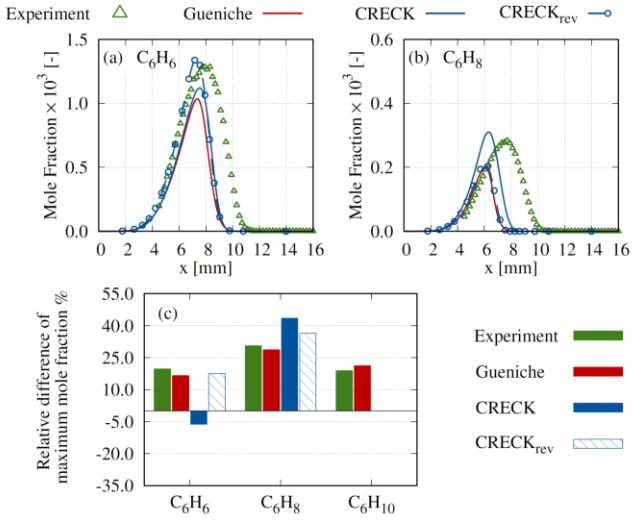

Fig. 11: Comparison between measured and modeled species profiles of Flame$_{CP}$: (a) benzene (C_6H_6) and (b) methylcyclopentadiene (C_6H_8); (c) relative difference of the mole fraction maxima between Flame$_{CP}$ and Flame$_{CPME}$ (%). The axial coordinate x represents the distance from the fuel outlet.

the discussed ring-enlargement route are affected by methane addition, thus showing the prominent role of these reactions in the formation of C_6 aromatics. Furthermore, the significant effect of the methyl radical, supports our initial assumption that a substantial amount of the C_6H_8 signal indeed corresponds to MCPT.

Figure11c also shows results for C_6H_{10}. Due to the large uncertainty on the isomeric composition, this species was not quantified, therefore for this comparison the recorded signal was depicted. However, given the relation between the raw signal and the mole fraction, and considering that the measurements at the same ionization energy were consecutively performed for the two flames, the ratio between the argon-normalized signal reflects the ratio between the mole fractions. As for C_6H_8, the increase induced by the methane addition supports the initial assumption of the presence of methylcyclopentene which would be formed by $C_5H_8 + CH_3$ followed by dehydrogenation.

Considering the numerical modeling, the observed trend for the C_6 species is correctly captured by the Gueniche model but not by the CRECK original mechanism. The CRECK$_{rev}$ version shows very good agreement with the experimental results (see Fig. 11c), because of the greater importance of the MCPT chemistry in the benzene formation. In fact, as shown in Fig. 12a and b, both propargyl and cyclopentadienyl radicals play significant roles in the two mechanisms to the formation of benzene, with a stronger contribution of the latter radical. The ROP analysis performed on both models reveals that the methyl-cyclopentadienyl route passing through the formation of the 2,5-cyclohexadienyl produces more than 15% of the overall benzene amount. In the original CRECK version, the role of this route, which was included with the reaction MCPT + H → $C_6H_6 + H_2$ + H, was significantly limited (6.1% contribution to benzene formation) while the propargyl contribution

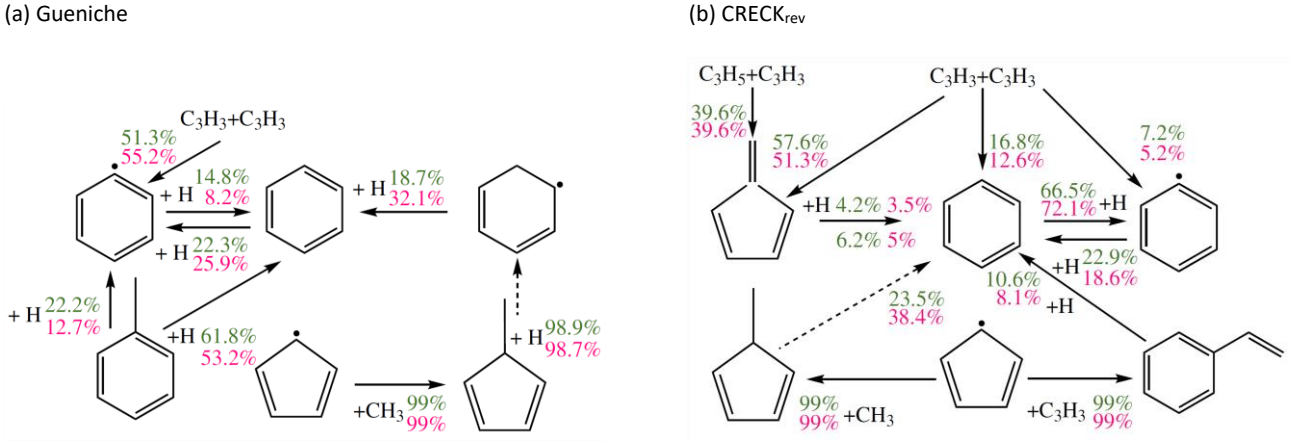

Fig. 12: Benzene formation sequences for the two models: (a) Gueniche and (b) CRECK$_{rev}$. The dashed lines summarize the reaction sequence presented in Fig. 3. To avoid ambiguity, in the figure, the relative contributions expressed in percent is intended as the contribution of a given reaction to the product as indicated by the direction of the arrow.

was stronger. To summarize, this rigorous combination of experimental and modeling work provides strong evidence concerning the importance of the RERs from C_5H_5 to C_6H_6 with the participation of the methyl radical.

In the continuation of this section, the corresponding "two-ring version" of this $C_5 \rightarrow C_6$ route, involving indene,[16] will be analyzed to understand the extent to which it affects naphthalene formation. This study will be carried out also considering different possible formation pathways, which specifically involve phenylacetylene (C_8H_6) and the dehydrogenation of $C_{10}H_{10}$. As for benzene, we will firstly comment on the experimental and numerical results for Flame$_{CP}$ and secondly, we will inspect the effect of methane addition in Flame$_{CPME}$.

The comparison between the measured and computed mole fraction profiles of C_8H_6, C_9H_8, and $C_{10}H_8$ is presented in Figs. 13a-c. Despite the pivotal role of $C_{10}H_{10}$, the quantified profile of this species is not shown here because of the large uncertainty on the most probable isomeric form. At this point, it should be mentioned again that, from a modeling perspective, the pathways related to C_7H_8, C_8H_6, C_8H_8, C_9H_8, and $C_{10}H_8$ were not modified. The observed differences between predictions with the CRECK and the CRECK$_{rev}$ mechanism are entirely attributable to the new rates calculated for C_5H_6, while the changes of the benzene and ethylbenzene pathways do not affect these results. C_9H_8 and $C_{10}H_8$ (Fig. 13b-c) are not included in the Gueniche model and therefore cannot be presented.

Regarding C_8H_6, the CRECK$_{rev}$ model shows an improved predictivity with respect to its original version. According to the CRECK mechanism C_8H_6 is mainly formed from styrene and styryl radical. Despite the very similar result, in the Gueniche mechanism the only formation pathway for this species is via $C_2H + C_6H_6 \rightleftarrows C_8H_6 + H$.

For indene, in the CRECK models its production occurs mostly via a series of reactions which concern oxidation products of naphthalene such as $C_{10}H_7O$, or decomposition of other larger species such as tetralin, which are formed from the naphthyl ($C_{10}H_7$) radical. In a second step, these molecules form the indenyl radical and ultimately indene via $H_2 + C_9H_7 \rightleftarrows H + C_9H_8$. Because of the decrease in naphthalene, the concentration of the indenyl radical in the CRECK$_{rev}$ model prediction is reduced by more than a factor of two. Nevertheless, this does not strongly affect the amount of

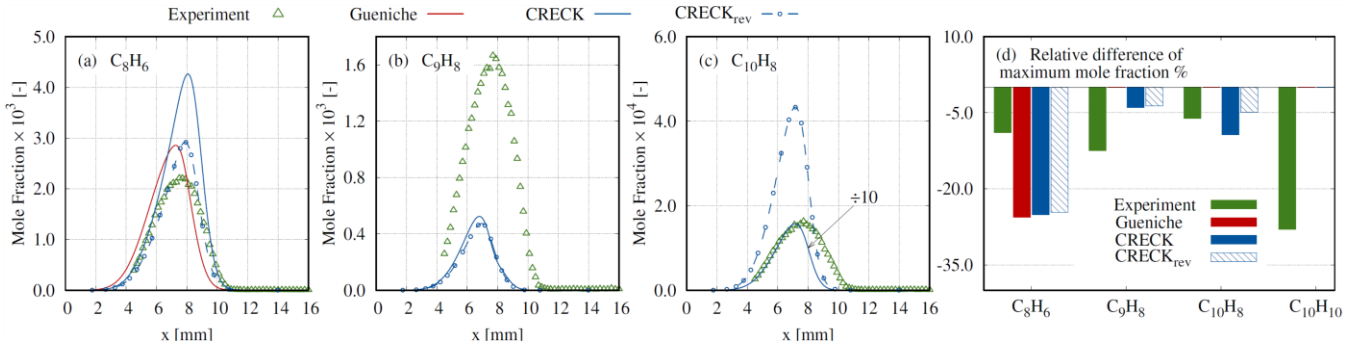

Fig. 13: Comparison between measured and computed aromatic species profiles from Flame$_{CP}$: (a) phenylacetylene (C_8H_6), (b) indene (C_9H_8), (c) naphthalene (C_8H_{10}), (d) relative difference of the mole fraction maxima between Flame$_{ME}$ and Flame$_{CPME}$ (%). The axial coordinate x represents the distance from the fuel outlet.

indene, because this decrease is compensated by a shift in the equilibrium indene production reaction towards the reactants.

For naphthalene, its production occurs via recombination of the cyclopentadienyl radical in both versions of the CRECK model.

In addition to the model indicating that the indenyl + CH_3 ⇄ naphthalene ring-enlargement reaction is not important under these conditions the experimental results may also provide evidence to support this conclusion. To this end, Figure 13d shows the trends in the $C_{10}H_8$ mole fractions upon methane addition compared with those of the species possibly involved in its formation: C_8H_6, C_9H_8, and $C_{10}H_{10}$. It is obvious that, in comparison to $Flame_{CP}$ the concentrations of these species in $Flame_{CPME}$ are reduced. This trend is opposite to what has been observed for benzene and supports the mechanistic insights that the formation of $C_{10}H_8$ would mostly depend on C_5H_5. However, these experimental results are consistent with the model predictions using the various mechanisms, i.e. the mechanisms predict a slight decrease in the concentrations of C_8H_6, C_9H_8, and $C_{10}H_8$ as well.

As can be seen in Fig. 13d, not all species diminish in the same amount. For the mole fractions of $C_{10}H_8$ and C_8H_6 this reduction is mostly in the order of 7-10%, while C_9H_8 manifests a stronger tendency and for $C_{10}H_{10}$ the measured decrease in concentration is above 25%. This extreme change is clearly correlated to the decreased C_5H_5 concentration and the C_5H_5 recombination reaction. Furthermore, it seems correlated to the almost equal increase in MCPT and a competition between these two pathways can be imagined. These experimentally observed tendencies could also imply the presence of multiple important formation mechanisms carrying a potential compensation effect. For example, mass growth sequences via acetylene addition reactions (HACA) could benefit from the increase in benzene and promote the formation of $C_6 \rightarrow C_8 \rightarrow C_{10}$ species such as phenylacetylene and naphthalene, which here appear to be less sensitive than others to the decrease of C_5H_5 amount. Additionally, the previously discussed methyl addition to indene could also play a role. However, given the complexity and the different pathways which could be involved, it is not possible to corroborate the importance of different formation routes for naphthalene except for that which passes via C_5H_5 recombination.

4.4 Second and third enlargement routes: $C_5H_5+C_2/C_3 \rightarrow C_7/C_8$

Despite the original intention of exploring the potential enlargement effect of methyl radical on cyclopentadienyl, we found out that interesting information about the role of C_5H_5 in the formation of C_7 and C_8 substituted aromatics could be drawn.

The possibility of ring-enlargement towards C_7 species from C_5H_5, has already been introduced in previous sections and principally focuses on acetylene addition to C_5H_5. The observation of intermediate radicals involved in these reactions, especially the c-C_7H_7 radical, could be rather challenging due to the difficulty to distinguish it from its more stable isomer benzyl, or possibly due to the existence of a high-temperature pathway which converts it into benzyl. However, some confirmation might come from the work of Hansen et al.[26] where cycloheptatriene (c-C_7H_8) and C_7H_6 five-membered ring species with side chains were identified in a low-pressure premixed flame; in addition, Savee et al.[18] identified c-C_7H_7 at 1000 K by employing tunable ionizing vacuum ultraviolet (VUV) radiation. An alternative route to form toluene was also proposed by Vervust et al.[71] where vinyl radical was added to C_5H_5.

In our study, the signal at *m/z*=92 was interpreted as toluene. As Fig. 14a shows, simulations performed with the Gueniche mechanism strongly overpredict the concentration of this species. As discussed above, this overprediction is due to the presence of the benzyl production channel $C_2H_2 + C_5H_5 \rightarrow C_7H_7$ (Eq. 4). In the CRECK models, the formation of toluene passes through the traditional methyl addition to phenyl (C_6H_5) radical, therefore the increase of benzene mole fraction connected to the kinetic updates (mostly the rates of Section 3.1) is reflected in toluene.

Quite surprisingly, the experimentally measured amount of toluene in the $Flame_{CPME}$ remains almost unchanged (Fig. 14d). This would have not been expected due to the combination of methane addition (which produces CH_3) and the augmented concentration of C_6H_6. A possible explanation of this result could lie in the role of C_5H_5. In fact, if for this fuel, the production of toluene involved the cyclopentadienyl radical then, as seen before, such a route would be less important in $Flame_{CPME}$. In this scenario, if the production of toluene would be promoted by the methane addition, whereas the

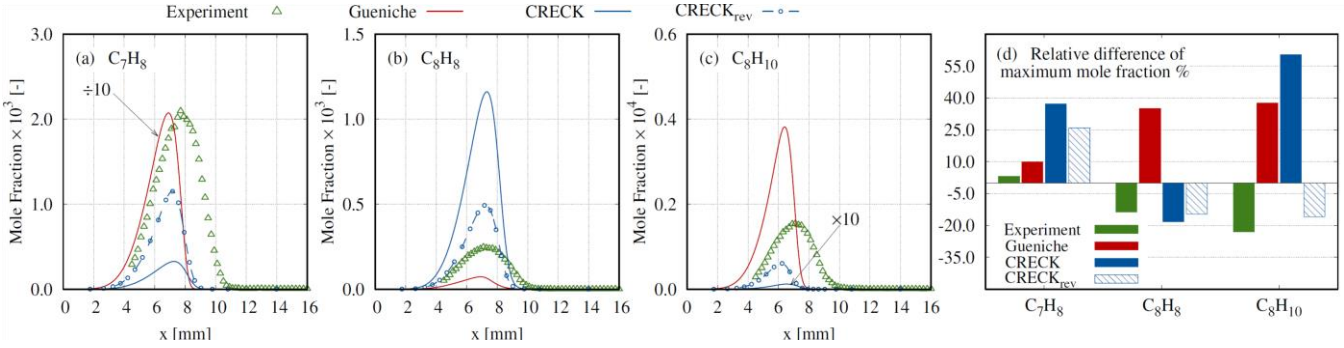

Fig. 14: Comparison between measured and computed aromatic species profiles from $Flame_{CP}$: (a) toluene (C_7H_8), (b) styrene (C_8H_8), (c) ethylbenzene (C_8H_{10}), and (d) relative difference of the mole fraction maxima between $Flame_{CP}$ and $Flame_{CPME}$ (%). The axial coordinate *x* represents the distance from the fuel outlet.

reduced concentration of C_5H_5 radical would hamper its formation, these effects would partly compensate. However, if new pathways for the formation of toluene should be possibly considered, a link between the chemistry of benzene (or phenyl) and toluene is certainly expected also for the flames considered here. In fact, the toluene-to-benzene maximum mole fraction ratio measured in this work agrees well with the value determined by an extensive comparative study performed by Hansen et al.[72]

Figures 14b-c depict the measured and computed concentration of C_8H_8 and C_8H_{10} in both flames. According to the Gueniche mechanism, styrene is mostly formed via dehydrogentation of C_8H_{10}, while in the CRECK model, the formation of C_8H_8 occurs almost entirely via $C_5H_5 + C_3H_3 \rightarrow C_8H_8$ whose rate was derived by Djokic et al.[53] in a work on C_5H_6 pyrolysis. Also, in this case, $CRECK_{rev}$ showed a significant improvement in predicting the experimental data.

The presence of a strong signal at *m/z*=106 can be related to different isomers. In Figure 14c, the contribution from all the species with such an elemental formula, and present in the mechanisms, is considered. In both cases, the most abundant species is ethylbenzene, which is formed via the second HAMA sequence: $C_7H_7 + CH_3 \rightarrow C_8H_{10}$. The large amount of benzyl radical, and therefore of toluene, explains why the Gueniche models predicts a value which is in good agreement with the experimental data. For the same reason, the numerically computed mole fraction is almost zero for the CRECK original model (Fig. 14d). In both cases, the amount of these aromatic species decreases upon addition of methane in $Flame_{CPME}$, which seems correlated to the fate of the C_5H_5 radical. Considering the large amount of allyl radical (a-C_3H_5) which might be present due to the fuel consumption sequence, we tested the effect of allyl addition to cyclopentadienyl using the CRECK mechanism. There have not been many dedicated studies about the reaction of C_5H_5 with allyl described in the literature. Lindstedt et al.[73] proposed a rate for the reaction $C_5H_5 + a\text{-}C_3H_5 \rightarrow C_8H_8 + H_2$ and a similar, although more detailed, reaction chain has been presented by Herbinet et al.[23]

During this work, owing to the above-discussed reaction which is responsible for styrene formation in the CRECK model, we hypothesize the occurrence of a similar reaction which could produce ethylbenzene $C_5H_5 + a\text{-}C_3H_5 \rightarrow C_8H_{10}$ (see Section 3.2). It is clear to us that this might be just a simplification and that other possible reactions could involve for example C_5H_7 radicals. However, it is also evident that C_8H_{10} follows quite clearly the trend of those species which rely on C_5H_5 as building block for their formation, such as styrene or $C_{10}H_{10}$, which was presented in Section 4.3.

A summary of the species analyzed in this work is provided in Figs. 15a-b, where also the largest detected species (*m/z*=202) is added as a representative of all the other larger intermediates which were not shown but follow the same trend.

5. Conclusions

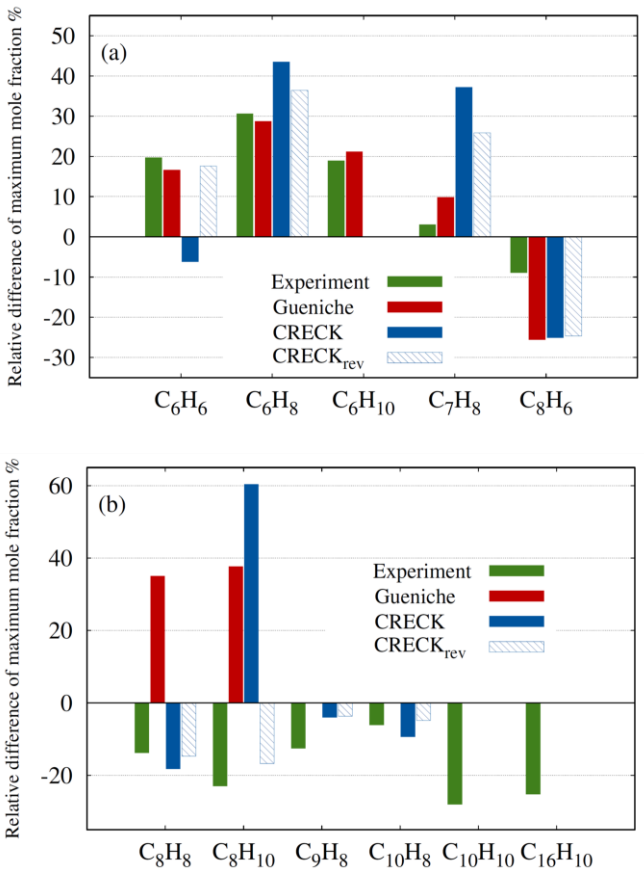

Fig. 15: Relative differences between the mole fraction maxima (%) in $Flame_{CP}$ and $Flame_{CPME}$ of the aromatic species discussed in this work.

In this work, the role of cyclopentadienyl in ring-enlargement reactions is investigated by probing the chemistry of a controlled flame environment.

The first flame, fueled with cyclopentene, serves as a baseline, while in a second flame, methane is added in replacement of the argon dilution. The obtained mass spectra show a significant sooting tendency for this fuel, as signals corresponding to C_{16} hydrocarbons were recorded. Mole fraction profiles of the main stable fuel intermediates and several aromatics were quantified, thus enabling a relative comparison between the two flames. To assist the interpretation of the experimental results and provide a bridge towards practical applications, this study comprises also a theoretical and modeling component, which includes quantum chemistry calculations and the introduction of new pathways which are responsible for cyclopentadienyl-driven molecular growth routes. The most relevant findings of this work are summarized in the following:

- A significant amount of cyclopentadiene is produced which, by undergoing H abstraction, can generate a large cyclopentadienyl radical-pool; this conclusion is experimentally supported by the prominent C_6H_8 and $C_{10}H_{10}$ peaks, which

suggest the occurrence of reactions in which cyclopentadienyl participates together with the methyl radical or by self-recombination.

- Upon methane addition, the concentrations of C_6 intermediates increase, thus supporting the identification of methylcyclopentadiene as one of the products corresponding to C_6H_8. An observed larger benzene concentration demonstrates the importance of the $C_5H_5 + CH_3$ route.
- An unchanged toluene amount and a general decrease in species with more than seven carbon atoms is observed after methane is added to the base flame. This fact is correlated to the decrease of the C_5H_8 reactivity upon addition of methane and implies a direct participation of cyclopentadienyl radical in RERs such as $C_5H_5 + C_3H_3$, $C_5H_5 + C_3H_5$, and $C_5H_5 + C_2H_2$ to produce styrene, ethylbenzene, and possibly toluene.
- The formation of naphthalene is dominated by the $C_5H_5 + C_5H_5$ route and is therefore hindered by the decrease in C_5H_5 concentration in the flame where methane is present. No strong effect of ring-enlargement from indenyl or of HACA pathways is observed. The decrease in larger PAHs is also likely to be caused by a decrease of naphthalene, which is acting as building block.
- While leaving the fuel-specific chemistry substantially unaltered, numerical simulations performed with the updated chemical mechanism show a significant improvement in the prediction of the aromatic species both on quantitative and on relative terms in comparison to the base flame.

Conflicts of interest

There are no conflicts to declare

Acknowledgements

The authors gratefully acknowledge financial support by the Deutsche Forschungsgemeinschaft (DFG, German Research Foundation)-Projektnummer 215035359-TRR 129. MB additionally thanks Dr. Warumporn Pejpichestakul and Dr. Matteo Pelucchi for providing the mechanism and their time for constructive discussions. NH acknowledges support from the U.S. DOE, Office of Science, Office of Basic Energy Sciences. Sandia National Laboratories is a multi-mission laboratory managed and operated by National Technology and Engineering Solutions of Sandia, LLC., a wholly owned subsidiary of Honeywell International, Inc., for the U.S. DOE National Nuclear Security Administration under contract DE-NA0003525.

Notes and references

1 A. G. G. M. Tielens, *Annu. Rev. Astron. and Astr.*, 2008, **46,** 289-337.
2 Y. Wang and S. H. Chung, *Prog. Energy Combust. Sci.*, 2019, **74,** 152-238.
3 B. D. Adamson, S. A. Skeen, M. Ahmed and N. Hansen, *J. Phys. Chem. A*, 2018, **122,** 9338-9349.
4 A. D'Anna, M. Commodo, M. Sirignano, P. Minutolo and R. Pagliara, *Proc. Combust. Inst.*, 2009, **32,** 793-801.
5 E. Michoulier, J. A. Noble, A. Simon, J. Mascetti and C. Toubin, *Phys. Chem. Chem. Phys.*, 2018, **20,** 8753-8764.
6 C. S. McEnally, L. D. Pfefferle, B. Atakan and K. Kohse-Höinghaus, *Prog. Energy Combust. Sci.*, 2006, **32,** 247-294.
7 A. M. Mebel and V. V. Kislov, *J. Phys. Chem. A*, 2009, **113,** 9825-9833.
8 D. Wang, A. Violi, D. H. Kim and J. A. Mullholland, *J. Phys. Chem. A*, 2006, **110,** 4719-4725.
9 C. Cavallotti and D. Polino, *Proc. Combust. Inst.*, 2013, **34,** 557-564.
10 C. Cavallotti, D. Polino, A. Frassoldati and E. Ranzi, *J. Phys. Chem. A*, 2012, **116,** 3313-3324.
11 V. V. Kislov and A. M. Mebel, *J. Phys. Chem. A*, 2008, **111,** 9532-9543.
12 A. E. Long, S. S. Merchant, A. G. Vandeputte, H. H. Carstensen, A. J. Vervust, G. B. Marin, K. M. V. Geem and W. H. Green, *Combust. Flame*, 2018, **187,** 247-256.
13 C. F. Melius, M. E. Colvin, N. M. Marinov, W. J. Pitz and S. M. Senkan, *Proc. Combust. Inst.*, 1996, **26,** 685-692.
14 L. V. Moskaleva, A. M. Mebel and M. C. Lin, *Proc. Combust. Inst.*, 1996, **26,** 521-526.
15 A. Laskin and A. Lifshitz, *Proc. Combust. Inst.*, 1998, **27,** 313-320.
16 L. Zhao, R. Kaiser, W. Lu, B. Xu, M. Ahmed, A. N. Morzov, A. M. Mebel, A. H. Howlader and S. F. Wnuk, *Nat. Commun.*, 2019, **10,** 3689.
17 S. Fascella, C. Cavallotti, R. Rota and S. Carrà, *J. Phys. Chem. A.*, 2005, **109,** 7546-7557.
18 J. D. Savee, T. M. Selby, O. Welz, C. A. Taatjes and D. L. Osborn, *J.Phys. Chem. Lett.*, 2015, **6,** 4153-4158.
19 C. Cavallotti, S. Mancarella, R. Rota and S. Carrá, *J. Phys. Chem. A*, 2007, **111,** 3959-3969.
20 S. Sharma, M. R. Harper and W. H. Green, *Combust. Flame*, 2010, **157,** 1331-1345.
21 K. D. King, *Int. J. Chem. Kinet.*, 1978, **10,** 117-123.
22 D. K. Lewis, M. Sarr and M. Keil, *J. Phys. Chem.*, 1974, **78,** 436-439.
23 O. Herbinet, A. Rodriguez, B. Husson, F. Battin-Leclerc, Z. Wang, Z. Cheng and F. Qi, *J. Phys. Chem. A*, 2016, **120,** 668-682.
24 C. S. McEnally and L. D. Pfefferle, *Combust. Sci. Technol.*, 1998, **131,** 323-344.
25 H. A. Gueniche, P. A. Glaude, R. Fournet and F. Battin-Leclerc, *Combust. Flame*, 2008, **152,** 245-261.
26 N. Hansen, T. Kasper, S. J. Klippenstein, P. R. Westmoreland, M. E. Law, C. A. Taatjes, K. Kohse-Höinghaus, J. Wang and T. A. Cool, *J. Phys. Chem. A*, 2007, **19,** 4081-4092.
27 M. Kamphus, M. Braun-Unkhoff and K. Kohse-Höinghaus, *Combust. Flame*, 2008, **152,** 28-59.
28 A. Lamprecht, B. Atakan and K. Kohse-Höinghaus, *Proc. Combust. Inst.*, 2000, **28,** 1817-1824.
29 D. Felsmann, H. Zhao, Q. Wang, I. Graf, T. Tan, X. Yang, E. A. Carter, Y. Ju and K. Kohse-Höinghaus, *Z. Phys. Chem.*, 2016, **230,** 1067-1097.
30 S. A. Skeen, B. Yang, H. A. Michelsen, J. A. Miller, A. Violi and N. Hansen, *Proc. Combust. Inst.*, 2013, **34,** 1067-1075.
31 K. Moshammer, L. Seidel, Y. Wang, H. Selim, S. M. Sarathy, F. Mauss and N. Hansen, *Proc. Combust. Inst.*, 2017, **36,** 947-955.

32 W. C. Wiley and I. H. McLaren, *Rev. Sci. Instrum.*, 1955, **26,** 1150-1157.
33 M. Baroncelli, D. Felsmann, N. Hansen and H. Pitsch, *Combust. Flame*, 2019, **204,** 320-330.
34 F. N. Egolfopoulos, N. Hansen, Y. Ju, K. Kohse-Höinghaus, C. K. Law and F. Qi, *Prog. Energy Combust. Sci.*, 2014, **43,** 36-67.
35 J. C. Biordi, *Prog. Energy Combust. Sci.*, 1977, **3,** 151-173.
36 Q. Mao, L. Cai and H. Pitsch, *https://arxiv.org/abs/1910.10970.*, 2019.
37 D. G. Truhlar, *Chem. Phys. Lett.*, 1998, **294,** 45-48.
38 L. G. Gao, J. Zheng, A. Fernández-Ramos, D. G. Truhlar and X. Xu, *J. Am. Chem. Soc.*, 2018, **140,** 2906-2918.
39 M. Pelucchi, C. Cavallotti, T. Faravelli and S. Klippenstein, *Phys. Chem. Chem. Phys.*, 2018, **20,** 10607-10627.
40 I. M. Alecu, J. Zheng, Y. Zhao and D. G. Truhlar, *J. Chem. Theory Comput.*, 2010, **6,** 2872-2887.
41 J. Zheng, I. M. Alecu, B. J. Lynch, Y. Zhao and D. G. Truhlar, Database of Frequency Scale Factors for Electronic Model Chemistries,Version 3 Beta 2., https://comp.chem.umn.edu/freqscale/version3b2.htm.
42 M. Frisch, G. W. Trucks, H. B. Schlegel, G. E. Scuseria, M. A. Robb, J. R. Cheeseman, G. Scalmani and V. Barone, Gaussian 09, revision D. 01, Gaussian, Inc., Wallingford CT, 2009.
43 T. Tan, X. Yang, Y. Ju and E. A. Carter, *Phys. Chem. Chem. Phys.*, 2016, **18,** 4594-4607.
44 T. Tan, X. Yang, C. M. Krauter, Y. Ju and E. A. Carter, *J. Phys. Chem. A*, 2015, **119,** 6377-6390.
45 A. Fernández-Ramos, J. A. Miller, S. J. Klippenstein and D. G. Truhlar, *Chem. Rev.*, 2006, **106,** 4518-4584.
46 Y. Georgievskii, J. A. Miller, M. P. Burke and S. J. Klippenstein, *J. Phys. Chem. A*, 2013, **117,** 12146-12154.
47 C. Eckart, *Phys. Rev.*, 1930, **35,** 1303-1309.
48 R. K. Robinson and R. P. Lindstedt, *Combust. Flame*, 2011, **158,** 666-686.
49 J. A. Miller and S. J. Klippenstein, *J. Phys. Chem. A*, 2003, **107,** 7783-7799.
50 L. V. Moskaleva and M. C. Lin, *Proc. Combust. Inst.*, 2002, **29,** 1319-1327.
51 J. L. Emdee, K. Brezinsky and I. Glassman, *J. Phys. Chem.*, 1992, **96,** 2151-2161.
52 X. Zhong and J. W. Bozzelli, *Int. J. Chem. Kin.*, 1997, **29,** 893-913.
53 M. R. Djokic, K. M. Van Geem, C. Cavallotti, A. Frassoldati, E. Ranzi and G. B. Marin, *Combust. Flame*, 2014, **161,** 2739-2751.
54 K. Narayanaswamy, H. Pitsch and P. Pepiot, *Combust. Flame*, 2015, **162,** 1193-1213.
55 W. Pejpichestakul, E. Ranzi, M. Pelucchi, A. Frassodati, A. Cuoci and T. Faravelli, *Proc. Combust. Inst.*, 2019, **37,** 1013-1021.
56 O. Herbinet, *personal communication*, 2018.
57 A. Ciajolo, A. Tregrossi, M. Mallardo, T. Faravelli and E. Ranzi, *Proc. Combust. Inst.*, 2009, **32,** 585-591.
58 H. Pitsch, FlameMaster: A C++ Computer Program for 0D Combustion and 1D Laminar Flame Calculations, 1993.
59 R. Seiser, H. Pitsch, K. Seshadri, W. J. Pitz and H. J. Gurran, *Proc. Combust. Inst.*, 2000, **28,** 2029-2037.
60 J. Wullenkord, I. Graf, M. Baroncelli, D. Felsmann, L. Cai, H. Pitsch and K. Kohse-Höinghaus, *Combust. Flame*, 2020, **212,** 323-336.
61 R. G. Butler and I. Glasmann, *Proc. Combust. Inst.*, 2009, **32,** 395-402.
62 C. Ji, R. Zhao, B. Li and F. N. Egolfopoulos, *Proc. Comb. Inst.*, 2013, **34,** 787-794.
63 N. Hansen, M. Schenk, K. Moshammer and K. Kohse-Höinghaus, *Combust. Flame*, 2017, **180,** 250-261.
64 L. Ruwe, K. Moshammer, N. Hansen and K. Kohse-Höinghaus, *Phys. Chem. Chem. Phys.*, 2018, **20,** 10780-10795.
65 N. Hansen, J. A. Miller, P. R. Westmoreland, T. Kasper, K. Kohse-Höinghaus, J. Wang and T. A. Cool, *Combust. Flame*, 2009, **156,** 2153-2164.
66 M. Zeng, J. Wullenkord, I. Graf and K. Kohse-Höinghaus, *Combust. Flame*, 2017, **184,** 41-54.
67 F. Carbone and A. Gomez, *Combust. Flame*, 2013, **161,** 453-464.
68 U. Struckmeier, A. Lucassen, N. Hansen, T. Wada, N. Peters and K. Kohse-Höinghaus, *Combust. Flame*, 2010, **157,** 1966-1975.
69 N. Hansen, J. A. Miller, S. J. Klippenstein, P. R. Westmoreland and K. Kohse-Höinghaus, *Combust. Explos. Shock Waves*, 2012, **48,** 508-515.
70 J. A. Miller, J. P. Senosiain, S. J. Klippenstein and Y. Georgievskii, *J. Phys. Chem. A*, 2008, **112,** 9429-9438.
71 A. J. Vervust, M. R. Djokic, S. S. Merchant, H. H. Carstensen, A. E. Long, G. B. Marin, W. H. Green and K. M. Van Geem, *Energy Fuels*, 2018, **32,** 3920-3934.
72 N. Hansen, X. He, R. Griggs and K. Moshammer, *Proc. Combust. Inst.*, 2018, **37,** 743-750.
73 P. Lindstedt, L. Maurice and M. Meyer, *Faraday Discuss.*, 2002, **119,** 409-432.